optica

Gating attosecond pulses in a noncollinear geometry: supplementary material

M. Louisy*,1, C.L. Arnold*,1, M. Miranda[1], E. W. Larsen[1], S. Bengtsson[1], D. Kroon[1], M. Kotur[1], D. Guénot[1], L. Rading[1], P. Rudawski[1], F. Brizuela[1], F. Campi[1], B. Kim[1], A. Jarnac[2], A. Houard[2], J. Mauritsson[1], P. Johnsson[1], A. L'Huillier[1], and C. M. Heyl[1]

[1] Department of Physics, Lund University, P. O. Box 118, SE-221 00 Lund, Sweden
[2] Laboratoire d'Optique Appliquée, ENSTA Paristech, École Polytechnique, CNRS, FR-91762 Palaiseau, France

Published 17 June 2015

This document provides supplementary information to "Gating attosecond pulses in a non-collinear geometry", http://dx.doi.org/10.1364/optica.2.000563. We give detailed information about the laser pules used in the experiment including a description of the CEP stabilization scheme, the pulse post-compression method and the pulse characterization. Finally, simulations of the driving field in a noncollinear geometry are provided, showing the dependence of the angular streaking process on the delay between the two driving pulses and on their CEP.

http://dx.doi.org/10.1364/optica.2.000563.s001

1. LASER PULSE DETAILS

A. CEP stabilization

The CEP is stabilized with a commercial f-2f interferometer (Menlo Systems) at the output of the laser using a slow feedback loop to an acousto-optical programmable filter (DAZZLER). The observed residual CEP fluctuations are most likely induced by pointing instabilities dynamically changing the coupling into the hollow capillary as well as by pulse to pulse energy fluctuations inside the capillary [1, 2]. The CEP stability on-target can in the future be strongly improved by implementing a fast pointing stabilization for the coupling into the capillary as well as by stabilizing the CEP behind the capillary in single-shot [3].

B. Pulse post-compression

Few-cycle pulses are obtained by post-compression using a hollow capillary [4] of 1 m length and 250 μm diameter, operated at 3 bars of He in differential pumping configuration [5]. Pulses with an energy of approximately 2.5 mJ and a pulse duration of 20 fs are focused into the entrance of the capillary and 0.9 mJ are obtained at the output (transmission approx. 40%). Behind the capillary the pulses are collimated with a f = 1.25 m focal length spherical mirror and compressed with chirped mirrors in double-angle configuration (Ultrafast Innovations). A pair of motorized fused silica wedges is used for dispersion fine control and temporal characterization. Initial pulse measurements showed sub-4 fs (FWHM) with residual third-order spectral phase and distinct temporal satellites. If glass wedges and chirped mirrors are used for post-compression, third- and higher-order spectral phase contributions usually remain uncompensated. By introducing a water-filled cell of matched length (here 5 mm) into the beam path, an additional degree of freedom is obtained due to a different ratio between second- and third-order dispersion for water as compared to the typical glasses used for wedges [6].

With both second- and third-order phases compensated, a relatively clean pulse of 3.2 fs (Fourier limit 2.9 fs) at a carrier wavelength of 720 nm is obtained with only small satellites [see Fig. S1 (c)]. The pulse energy after compression is $\sim$ 0.5 mJ.

C. Pulse characterization

The pulses are characterized with the d-scan technique consisting of recording frequency doubled spectra as a function of dispersion (glass insertion of the wedges) and retrieving iteratively the spectral phase from the measured fundamental and second harmonic generation spectra [7] [Fig. S1].

2. ANGULAR STREAKING SIMULATIONS

The delay-dependent XUV emission characteristics [Fig. 2(a) in the main Letter] can be better understood with the help of an angular electric field distribution map where the absolute value of the total electrical field on axis, $E = E_1 + E_2$ with

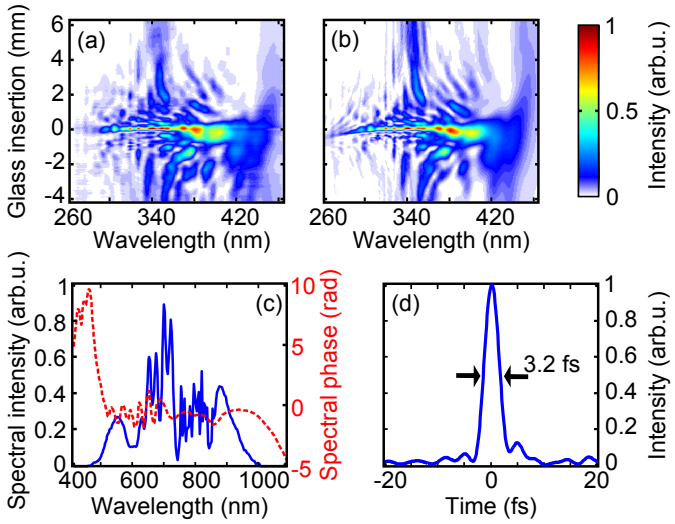

Fig. S1. Pulse characterization. (a) Measured d-scan. (b) Retrieved d-scan. (c) Measured spectral profile (solid line) and retrieved spectral phase (red dashed line). (d) Retrieved temporal profile.

$E_{1,2} = \mathcal{E}_{1,2}\exp[i(\omega t \pm \Delta t/2) + \phi_{CE}^{1,2}]$ is plotted as a function of Δt and β. $\phi_{CE}^{1,2}$ denote the CEPs for the two laser pulses. We consider a Gaussian envelope $\mathcal{E}_{1,2} = \exp[-2\ln(2)(t \pm \Delta t/2)^2/\tau^2]$.

Fig. S2 (b-d) shows examples of such angular electric field distribution maps together with an illustration of the mapping process [Fig. S2 (a)]. Each vertical line-out in these figures represents the angular electrical field distribution $|\Re[E(\beta)]|$, i.e. its temporal distribution $|\Re[E(t)]|$ mapped onto the emission angle, as illustrated in Fig. S2 (a) for $\Delta t = T$. Three different angular electric field distribution maps are shown, mimicking the experimental conditions and illustrating the influence of a shift of the CEP of one or both driving pulses on the mapping process.

The angular electric field distribution indicates the orientation of the wave fronts of the total electrical field on the optical axis, determining directly the XUV emission angles. Note that the XUV emission direction is not necessarily identical with the wave front orientation angle. This is due to a delay between the maximum of the laser field cycle and the XUV emission time. For $\phi_{CE}^2 = \phi_{CE}^1$, field maxima close to $\beta = 0$ occur for delays equal to an integer number of cycles ($\Delta t = \pm nT$). This corresponds to a total relative phase between the two fields at the point of intersection equal to zero (modulo 2π), such that the transversal intensity grating has a maximum on the optical axis [see Fig. 1 (c) in the main Letter]. For $|\Delta t| \approx T$, most interesting for gating in our experimental conditions, several distinct maxima are visible along β, indicating the orientations of the wave fronts of consecutive half-cycles. For larger delays $|\Delta t| \approx nT$, where n is an integer, the angular rotation between consecutive half-cycles is increased but at the same time the field intensity is reduced significantly, leading to only weak XUV emission. For delays such that $\Delta t = (n + 1/2)\,T$, the partially overlapped laser pulses interfere destructively on the optical axis, resulting in two weaker off-axis maxima in the transversal intensity grating which form multiple harmonic sources [8], leading to a reduced XUV emission and interference effects which suppress efficient gating [9].

As discussed in the main Letter, the angular streaking process is strongly CEP-dependent. The effect is clearly visible in

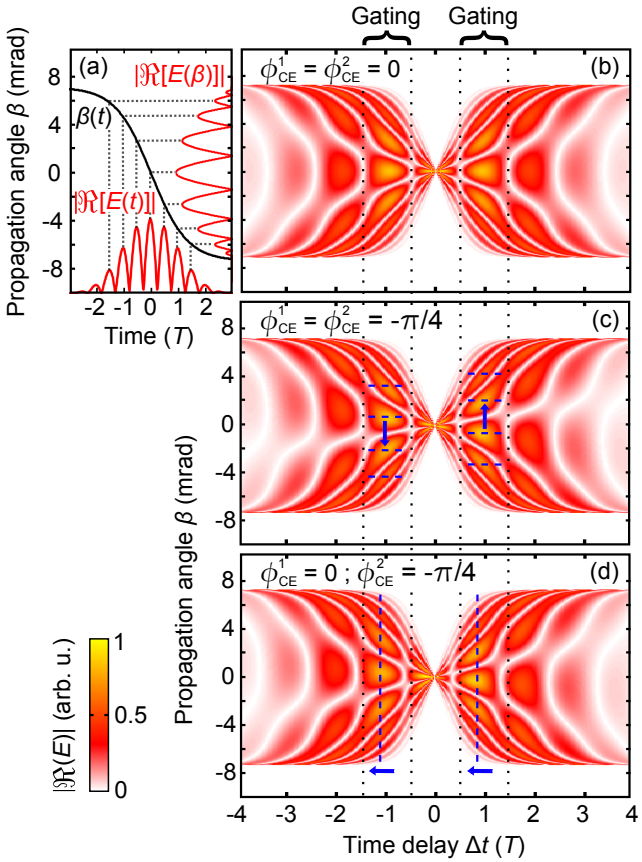

Fig. S2. Angular electric field distribution maps (b-d) displaying $|\Re[E(\Delta t, \beta)]|$, indicating the orientation of individual half-cycle wave fronts as a function of the time delay for $\phi_{CE}^{1,2} = 0$ (b), $\phi_{CE}^{1,2} = -\pi/4$ (c) and $\phi_{CE}^1 = 0$; $\phi_{CE}^2 = -\pi/4$ (d). The blue arrows in (c) and (d) indicate the pattern movement with decreasing CEP. The side panel (a) shows $|\Re[E(t)]|$ and the corresponding $|\Re[E(\beta)]|$ for $\Delta t = T$ together with the time-to-angle mapping function $\beta(t)$.

Fig. S2 (c). The maxima in the angular electric field distribution map shift with CEP (in different directions for positive and negative delay) and consequently the XUV emission angle changes. Gating is also possible for $\phi_{CE}^1 \neq \phi_{CE}^2$. In this case, it does not occur for delays equal to multiples of T and the symmetry between positive and negative delays is lost [Fig. S2 (d)].

* These authors contributed equally to this work.

REFERENCES

1. H. Wang, M. Chini, E. Moon, H. Mashiko, C. Li, and Z. Chang, "Coupling between energy and phase in hollow-core fiber based f-to-2f interferometers," Opt. Express **17**, 12082–12089 (2009).
2. F. Lücking, A. Trabattoni, S. Anumula, G. Sansone, F. Calegari, M. Nisoli, T. Oksenhendler, and G. Tempea, "In situ measurement of nonlinear carrier-envelope phase changes in hollow fiber compression," Opt. Lett. **39**, 2302–2305 (2014).
3. T. Fordell, M. Miranda, C. L. Arnold, and A. L'Huillier, "High-speed carrier-envelope phase drift detection of amplified laser pulses," Opt. Express **19**, 23652–23657 (2011).
4. M. Nisoli, S. De Silvestri, O. Svelto, R. Szipöcs, K. Ferencz,

C. Spielmann, S. Sartania, and F. Krausz, "Compression of high-energy laser pulses below 5 fs," Opt. Lett. **22**, 522–524 (1997).

5. A. Suda, M. Hatayama, K. Nagasaka, and K. Midorikawa, "Generation of sub-10-fs, 5-mj-optical pulses using a hollow fiber with a pressure gradient," Appl. Phys. Lett. **86**, 111116 (2005).
6. F. Silva, M. Miranda, B. Alonso, J. Rauschenberger, V. Pervak, and H. Crespo, "Simultaneous compression, characterization and phase stabilization of GW-level 1.4 cycle VIS-NIR femtosecond pulses using a single dispersion-scan setup," Opt. Express **22**, 10181–10191 (2014).
7. M. Miranda, T. Fordell, C. Arnold, A. L'Huillier, and H. Crespo, "Simultaneous compression and characterization of ultrashort laser pulses using chirped mirrors and glass wedges," Opt. Express **20**, 688 (2012).
8. C. M. Heyl, P. Rudawski, F. Brizuela, S. Bengtsson, J. Mauritsson, and A. L'Huillier, "Macroscopic effects in noncollinear high-order harmonic generation," Physical Review Letters **112**, 143902 (2014).
9. C. M. Heyl, S. N. Bengtsson, S. Carlström, J. Mauritsson, C. L. Arnold, and A. L'Huillier, "Noncollinear optical gating," New Journal of Physics **16**, 052001 (2014).